REPORT DOCUMENTATION PAGE

Public Reporting burden for this collection of information is estimated to average 1 hour per response, including the time for reviewing instructions, searching existing data sources, gathering and maintaining the data needed, and completing and reviewing the collection of information. Send comment regarding this burden estimates or any other aspect of this collection of information, including suggestions for reducing this burden, to Washington Headquarters Services, Directorate for information Operations and Reports, 1215 Jefferson Davis Highway, Suite 1204, Arlington, VA 22202-4302, and to the Office of Management and Budget, Paperwork Reduction Project (0704-0188,) Washington, DC 20503.

1. AGENCY USE ONLY (Leave Blank)	2. REPORT DATE 5-19-2006	3. REPORT TYPE AND DATES COVERED Final Report 01 Oct 06 - 30 Jun 07

4. TITLE AND SUBTITLE	5. FUNDING NUMBERS
Flexible Soldier and Machine Interface for Micro Air Vehicles	C W 9 1 1 N F - 0 6 - 1 - 0 4 7 3

6. AUTHOR(S)
Mark Costello, Eric Beyer

7. PERFORMING ORGANIZATION NAME(S) AND ADDRESS(ES)	8. PERFORMING ORGANIZATION REPORT NUMBER
Georgia Tech Research Corp. 505 10th Street, NW Atlanta, GA 30332-0420	

9. SPONSORING / MONITORING AGENCY NAME(S) AND ADDRESS(ES)	10. SPONSORING / MONITORING AGENCY REPORT NUMBER
U. S. Army Research Office P.O. Box 12211 Research Triangle Park, NC 27709-2211	5 1 4 2 8 . 1 - C I - I I

11. SUPPLEMENTARY NOTES
The views, opinions and/or findings contained in this report are those of the author(s) and should not be construed as an official Department of the Army position, policy or decision, unless so designated by other documentation.

12 a. DISTRIBUTION / AVAILABILITY STATEMENT	12 b. DISTRIBUTION CODE
Approved for public release; distribution unlimited.	.

13. ABSTRACT (Maximum 200 words)

The work reported here focused on the creation of a user friendly and flexible connection between the autopilot a micro air vehicle and a laptop computer based ground station, and deployment of this environment to a micro air vehicle research flight test program. The objective in creating the ground station Graphical User Interface (GUI) was to provide basic connectivity to the air vehicle sensor suite. This includes the ability to send and receive control parameters, servo calibration parameters, sensor calibration parameters, and mission waypoints. Another objective of the autopilot interface is to connect it with the FalconView software package so route waypoints can be defined and current GPS fixes can be plotted on a map. It is also desirable to display time history data in real time as it is received. The objective to employ the developed interface to a micro air vehicle test program was fulfilled during a parafoil and payload micro air vehicle test program. The developed GUI was employed successfully on an autonomous parafoil airdrop program where direct longitudinal control was achieved through dynamic incidence angle changes of the parafoil canopy. Addition of this extra control channel requires simple rigging changes and an additional servo actuator. A set of air drops from an altitude of around 300 m was performed to demonstrate and validate glide slope control authority using dynamic incidence angle control. The ability of dynamic incidence angle to alter the glide slope of a parafoil and payload aircraft was demonstrated through a flight test program with a micro parafoil system.

14. SUBJECT TERMS	15. NUMBER OF PAGES
Unmanned Air Vehicles, Parafoil, Flight Mechanics, Control	31
	16. PRICE CODE

Flexible Soldier and Machine Interface for Micro Air Vehicles

Mark Costello
Sikorsky Associate Professor
School of Aerospace Engineering
Georgia Institute of Technology
Atlanta, Georgia 30332

Eric Beyer
Graduate Research Assistant
School of Aerospace Engineering
Georgia Institute of Technology
Atlanta, Georgia 30332

The work reported here focuses on the creation of a user friendly and flexible connection between the autopilot of a micro air vehicle and a laptop computer based ground station, and subsequent deployment of this environment to a micro air vehicle research flight test program. The objective in creating the ground station Graphical User Interface (GUI) was to provide basic connectivity to the air vehicle sensor suite. This includes the ability to send and receive control parameters, servo calibration parameters, sensor calibration parameters, and mission waypoints. Another objective of the autopilot interface is to connect it with the FalconView software package so route waypoints can be defined and current GPS fixes can be plotted on a map. The developed GUI was employed successfully on an autonomous parafoil airdrop program where direct longitudinal control was achieved through dynamic incidence angle changes of the parafoil canopy. Addition of this extra control channel requires simple rigging changes and an additional servo actuator. A set of air drops from an altitude of around 300 m was performed to demonstrate and validate glide slope control authority using dynamic incidence angle control. The ability of dynamic incidence angle to alter the glide slope of a parafoil and payload aircraft was demonstrated through a flight test program with a micro parafoil system.

Nomenclature

b = Canopy span.

$\bar{c}$ = Canopy main chord.

C_{DS} = Payload drag coefficient.

$\bar{d}$ = Brake characteristic length.

$\vec{F}_W$ = Weight vector in a body reference frame.

$\vec{F}_S$ = Payload drag vector in a body reference frame.

$\vec{F}_A, \vec{M}_A$ = Aerodynamic force and moment vectors in a body reference frame.

$\vec{F}_{AM}, \vec{M}_{AM}$ = Apparent mass force and moment vectors in a body reference frame.

I_T = Inertia matrix of total system.

m = Mass of the combined system including payload and canopy.

p, q, r = Angular velocity components in a body reference frame.

$\tilde{p}, \tilde{q}, \tilde{r}$ = Angular velocity of the system in the canopy frame.

r_{LOS} = Line of site vector from parafoil to target.

S_ω^B, S_ω^C = Cross product matrix of the angular velocity expressed in a body and canopy reference frame.

$S_{CG,P}^B$ = Cross product matrix of the vector from the mass center to aerodynamic center.

$S_{CG,M}^B$ = Cross product matrix of the vector from the mass center to apparent mass center.

$S_{CG,C}^B$ = Cross product matrix of the vector from the mass center to canopy rotation point.

$S_{V_A}^C$ = Cross product matrix of the parafoil aerodynamic velcoity.

S_P, S_S = Reference area of the parafoil canopy and payload.

u, v, w = Velocity components of mass center in the body reference frame.

$\tilde{u}, \tilde{v}, \tilde{w}$ = Velocity components of the aerodynamic center in the canopy reference frame.

u_{SA}, v_{SA}, w_{SA} = Aerodynamic velocities of the payload in the body frame

$\vec{V}_{A/I}$ = Velocity vector of the wind in an inertial reference frame.

V_A, V_S = Total aerodynamic speed of the parafoil canopy and payload.

x, y, z = Inertial positions of the system mass center.

$\Delta x_c, \Delta y_c, \Delta z_c$ = Distance vector components from mass center to the canopy rotation point in a body reference frame.

$\Delta x_p, \Delta y_p, \Delta z_p$ = Distance vector components from the canopy rotation point to the aerodynamic center in a canopy reference frame.

Γ = Canopy incidence angle.

ϕ, θ, ψ = Euler roll, pitch and yaw angles.

θ_{LOS} = Angle of the line of site vector.

ω_{LOS} = Angular velocity of the line of sight vector.

I. Introduction

Efficient flight testing of new micro air vehicles requires useful feedback of the state of the air vehicle to aircraft operators. Over several years, a laptop based ground station connected to the aircraft's onboard autopilot has been developed and subsequently optimized. To make the ground station interface to the autopilot more useful, several substantial improvements have been made to the system and delivered to the U.S. Army Research Laboratory. The GUI interface developed under this project enables automation between the GUI and FalconView so route waypoints can be specified on a map and subsequently uploaded to the autopilot during a mission. The GUI allows the current position to be displayed on a FalconView map and saved so it can be played back at a latter time. The GUI also allows the received data to be plotted on chart as the data is received.

This GUI ground station and autopilot interface was employed in the flight testing of a new glide slope control mechanism for autonomous parafoils. Most autonomous parafoil and payload aircraft possess only lateral control, achieved by right and left parafoil brake deflection. Direct longitudinal control through dynamic incidence angle changes provides another control degree of freedom which is needed to improve impact point accuracy. Addition of this extra control channel requires simple rigging changes and an additional servo actuator. With the aid of the developed ground station GUI, the research conducted under this research program has established that the addition of direct glide path control enables impact point accuracy improvements of autonomous parafoil and payload aircraft by a factor of 3.

II. Ground Station Software

Ground station software can be very useful while operating micro air and ground vehicles. The ground station software developed here is based on a graphical user interface (GUI) shown in Figure 2 and was written in Visual Basic 2005. The GUI was designed to be user friendly and includes several new features which were lacking in previous versions.

The ground station software communicates with the autopilot via serial communication. The serial port is configured using the "Serial Port Configuration" window of the GUI (see Figure 1) and the connection can be toggled on or off. Once connected, the autopilot continuously sends information (sensor, control, and servo data) to the ground station which is displayed on the main page of the GUI (see Figure 1). The sensor data can also be plotted versus time (shown in Figure 3) by using the "Plot Data" functionality of the GUI. The data points are continuously updated as new information is received and the axes scale appropriately. The user can also open up FalconView through the ground station software, which will display the past and current latitude/longitude of the autopilot on a map of the user's choosing (assuming the autopilot has a GPS fix) as shown in Figure 4. All the sensor, control, and servo data can be recorded using the GUI's "Record" functionality. The recorded data is saved as .txt and .gps files which can be analyzed at a convenient time. The .gps file can be opened with FalconView and the "play-back" feature of FalconView allows the user to playback the trajectory (which is time stamped) on a map of their choosing.
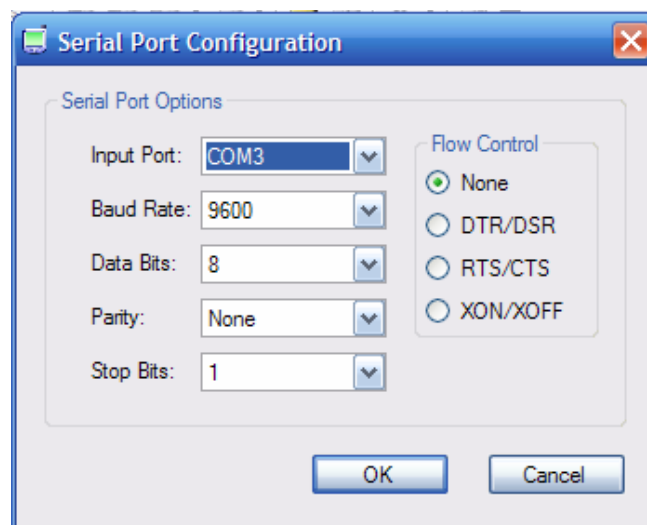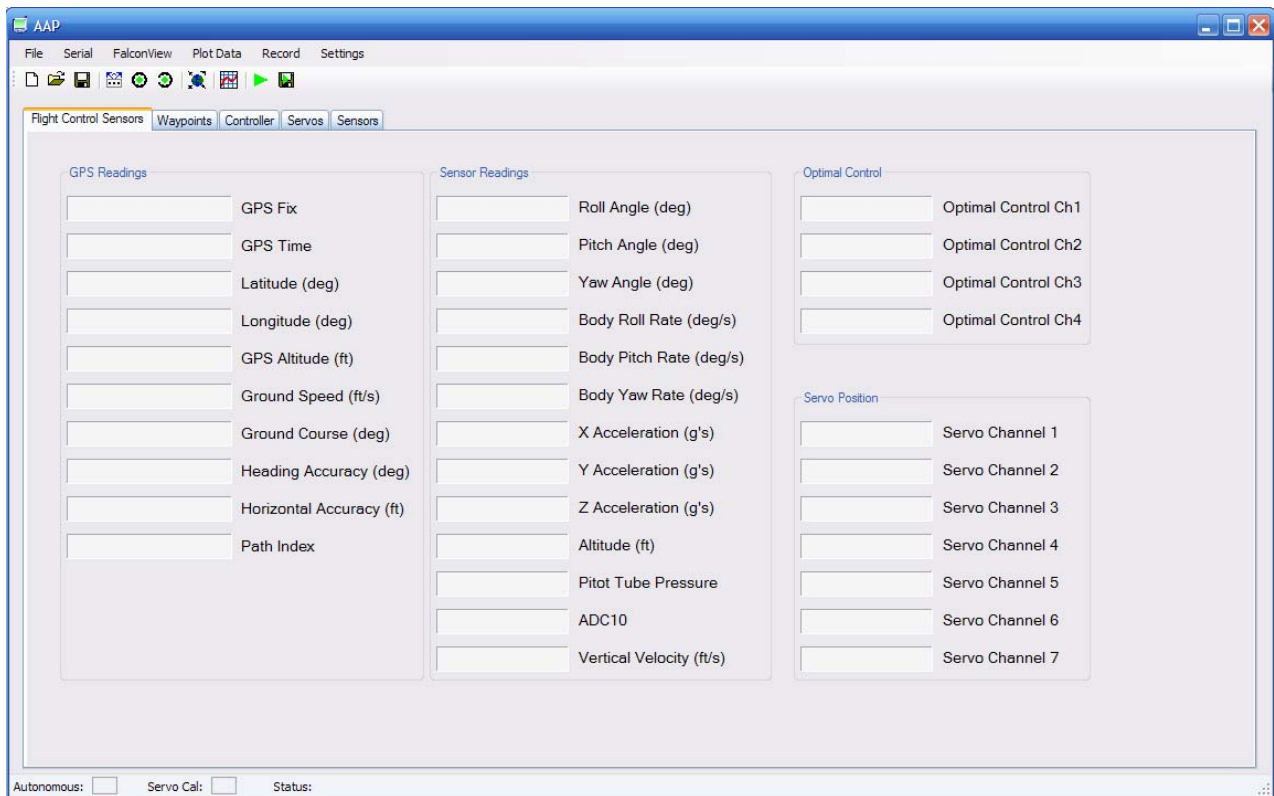

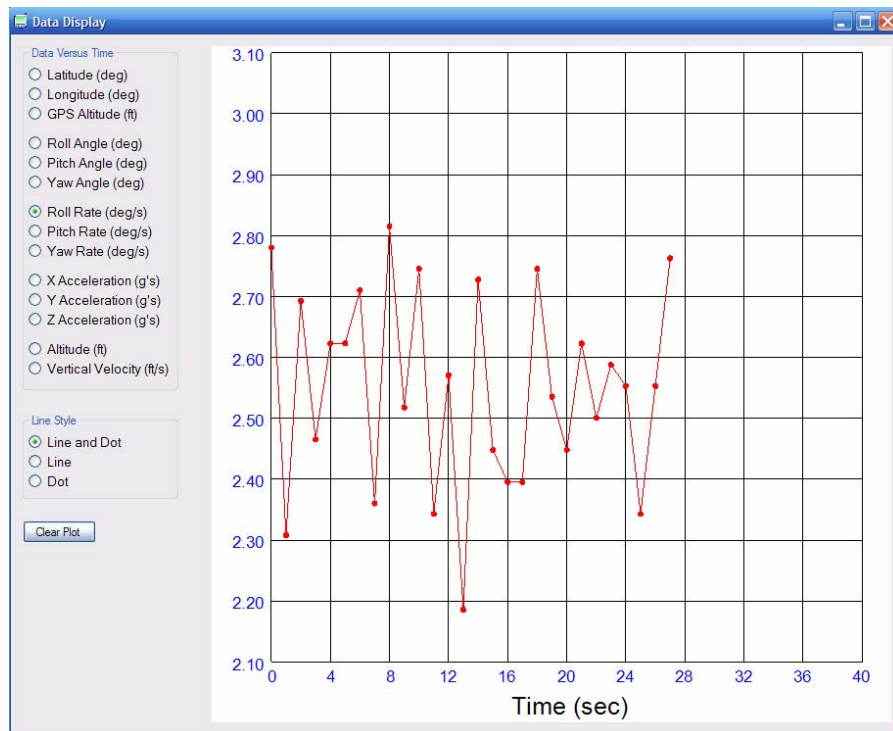Fig. 1 - Serial Port Communications

Fig. 2 – Graphical User Interface

Fig. 3 – Sensor Data Plotting
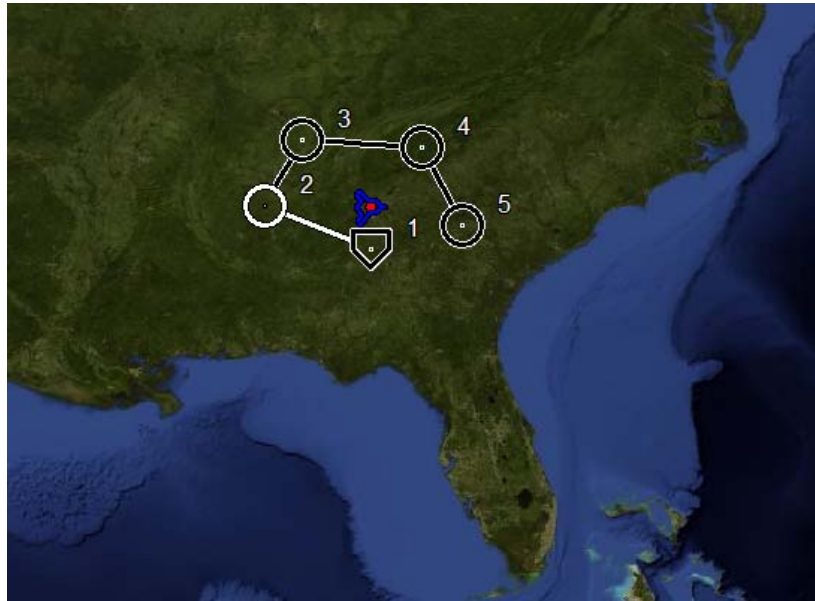
American Institute of Aeronautics and Astronautics

Fig. 4 – Falcon View Way Point Mapping

The autopilot can also be easily programmed using the ground station software. Control, sensor, and servo parameters can be sent to the autopilot using the "Controller", "Servos", and "Sensors" tab page shown in Figure 1. This allows the user to easily calibrate the autopilot to specific systems. Waypoints are sent in a similar manner to the autopilot using the "Waypoints" tab page. The user is able to manually enter waypoints (latitude, longitude, altitude, airspeed) through this interface or download prespecified waypoints from FalconView's Route Editor function as shown in Figure 4. This allows the waypoints to be easily created and changed to specific missions on an appropriate map.

III. Parafoil Glide Slope Control

Parafoil and payload systems are unique flight vehicles well suited to perform autonomous airdrop missions. These air vehicles are compact before parafoil deployment, lightweight, fly at low speed, and impact the ground with low velocity. The predominant control mechanism for parafoils is left and right brake deflection. When a right brake control input is executed, the right back corner of the parafoil canopy is pulled down by changing the length of the appropriate suspension lines. Canopy changes created by brake deflection subsequently cause predictable changes in aerodynamic loads which is leveraged for control of the vehicle. For most parafoils, deployment of the right brake causes a significant drag rise and a small lift increase on the right side of the parafoil canopy combined with slight right tilt of the canopy. The overall effect causes the parafoil to skid turn to the right when a right parafoil brake is activated.[1] Longitudinal control is more difficult to achieve. Ware and Hassell showed symmetric deflection of brakes to an angle of 45 degrees as pitch control did not effectively change the trim angle-of-attack; it did cause an increase in the lift and drag values at trim conditions, but the lift-drag ratio remained effectively unchanged.[2] Symmetric brake deflection to an angle of 90 degrees caused large changes in trim angle-of-attack with the canopy stalling reducing the lift-drag ratio to a value of about 0.5. Human sky divers use weight shift for both longitudinal and lateral control. By shifting weight fore and aft, glide slope can be actively controlled and permits accurate trajectory tracking, to include very accurate ground impact point control in the presence of relatively high atmospheric winds.

The bulk of current autonomous parafoil and payload aircraft employ right and left brake deflection for control which strictly speaking permits only lateral control. These aircraft typically do not have a direct means of longitudinal control. Hence, autonomous controllers for these air vehicles are greatly challenged to track three dimensional trajectories and impact a specific ground target point. The usual means to create some semblance of

5
American Institute of Aeronautics and Astronautics

altitude control is through a weaving maneuver back and forth across a desired trajectory path to "dump" altitude as progress is made along the desired path. [3-10] Near the intended ground impact location, current autonomous systems either spiral over the target or S-turn to the target. A key to the success for these algorithms is accurate descent rate estimation which is difficult to accomplish and prone to error.
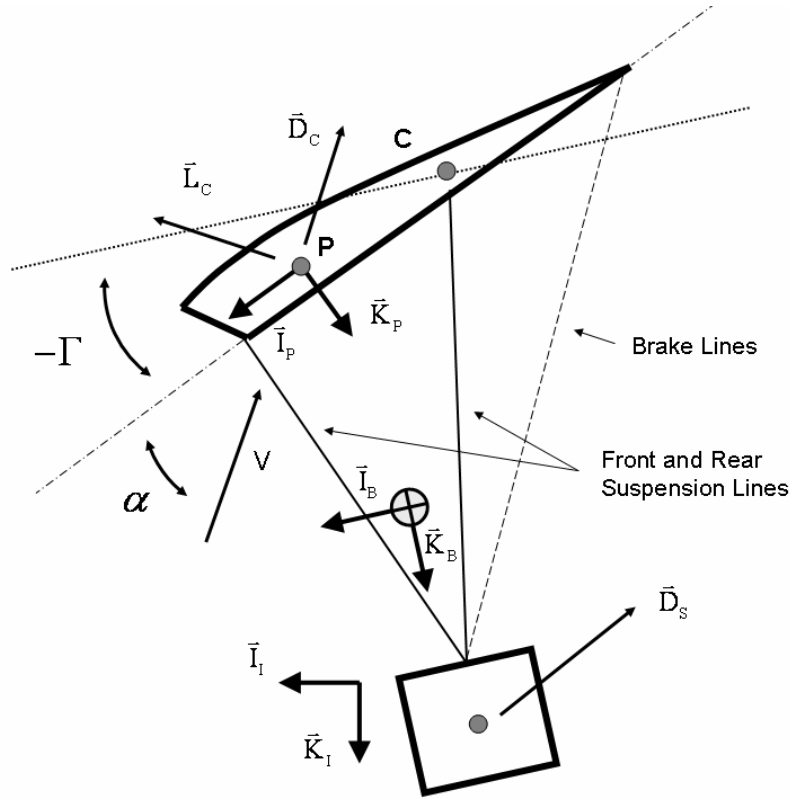

Fig. 5 Parafoil and Payload Schematic

The work reported here creates a glide slope control mechanism intended for use on autonomous parafoil and payload aircraft. Rather than using weight shift or symmetric brake deflection glide slope control is physically achieved by changing the longitudinal rigging of the parafoil and payload combination dynamically in flight. The extra degree of freedom of control requires simple rigging changes and the addition of one additional servo actuator to the system. A detailed description of the basic mechanical design of the glide slope control mechanism is provided below. Traditional parafoil dynamic models treat the canopy orientation fixed with respect to the payload.[11-14] These traditional models allow effects such as apparent mass to be easily incorporated. A new 6 degree-of-freedom model is created that include changing canopy orientation with respect to the payload and model apparent mass effects in a complete manner.

When combined with traditional right and left brake control, glide slope control is an attractive feature for autonomous parafoil and payload aircraft since it allows the flight control laws to directly correct descent rate thus eliminating the need for descent rate estimation and the resulting error induced into the final delivery error. The ability of this system to change glide slope in flight is demonstrated with flight test results for an exemplar micro parafoil and payload system. The micro parafoil and payload system is fitted with a data logger equipped with a sensor suite that contains GPS, accelerometers, gyroscopes, barometric altimeter, magnetometers, and servo position so that the complete state of the payload along with all control inputs can be recorded. These flight test results are subsequently synthesized and incorporated into a 6 degree-of-freedom parafoil simulation and autonomous performance with and without glide slope control is reported. Monte Carlo simulations are performed to predict impact point statistics using only lateral control, and lateral/longitudinal control. Results indicate that a dramatic improvement in impact point statistics is realized with the addition of glide slope control.

Figure 5 shows a schematic of a parafoil and payload system. With the exception of movable parafoil brakes, the parafoil canopy is considered to be a fixed shape once it has completely inflated. The combined system of the

parafoil canopy and the payload are modeled with 6 DOF, including three inertial position components of the total system mass center as well as the three Euler orientation angles. A body frame is fixed at the system mass center with I_B forward and aligned with the top of the payload. Orientation of the parafoil canopy with respect to the payload is defined as the incidence angle Γ and is considered a control variable. Rotation of the canopy about point C allows tilting of the canopy lift and drag vectors resulting in changes in the equilibrium glide slope. The canopy rotation point C is in line with the rear suspension lines so that by shorting the front lines and lengthening the brake lines a pure canopy rotation can be achieved. The aerodynamic center is defined as P.

The kinematic equations for the parafoil and payload system are provided in Eqs. (1) and (2). The common shorthand notation for trigonometric functions is employed where $\sin(\alpha) \equiv s_\alpha$, $\cos(\alpha) \equiv s_\alpha$ and $\tan(\alpha) \equiv t_\alpha$.

$$\begin{Bmatrix} \dot{x} \\ \dot{y} \\ \dot{z} \end{Bmatrix} = \left[T_{IB} \right]^T \begin{Bmatrix} u \\ v \\ w \end{Bmatrix} \tag{1}$$

$$\begin{Bmatrix} \dot{\phi} \\ \dot{\theta} \\ \dot{\psi} \end{Bmatrix} = \begin{bmatrix} 1 & s_\phi t_\theta & c_\phi t_\theta \\ 0 & c_\phi & -s_\phi \\ 0 & s_\phi/c_\theta & c_\phi/c_\theta \end{bmatrix} \begin{Bmatrix} p \\ q \\ r \end{Bmatrix} \tag{2}$$

The matrix T_{IB} represents the transformation matrix from an inertial reference frame to the body reference frame.

$$T_{IB} = \begin{bmatrix} c_\theta c_\psi & c_\theta s_\psi & -s_\theta \\ s_\phi s_\theta c_\psi - c_\phi s_\psi & s_\phi s_\theta s_\psi + c_\phi c_\psi & s_\phi c_\theta \\ c_\phi s_\theta c_\psi + s_\phi s_\psi & c_\phi s_\theta s_\psi - s_\phi c_\psi & c_\phi c_\theta \end{bmatrix} \tag{3}$$

The dynamic equations are formed by summing forces and moments about the system CG both in the body reference frame and equating to the time derivative of linear and angular momentum respectively.

$$\begin{Bmatrix} \dot{u} \\ \dot{v} \\ \dot{w} \end{Bmatrix} = \frac{1}{m} \left(\vec{F}_W + \vec{F}_A + \vec{F}_S + \vec{F}_{AM} \right) - S_\omega^B \begin{Bmatrix} u \\ v \\ w \end{Bmatrix} \tag{4}$$

$$\begin{Bmatrix} \dot{p} \\ \dot{q} \\ \dot{r} \end{Bmatrix} = \left[I_T \right]^{-1} \left(\vec{M}_A + \vec{M}_{AM} + S_{CG,P}^B \vec{F}_A + S_{CG,S}^B \vec{F}_S + S_{CG,M}^B \vec{F}_{AM} - S_\omega^B \left[I_T \right] \begin{Bmatrix} p \\ q \\ r \end{Bmatrix} \right) \tag{5}$$

The convention is used where the vector cross product of two vectors $\vec{r} = \{r_x \quad r_y \quad r_z\}^T$ and $\vec{F} = \{F_x \quad F_y \quad F_z\}^T$ both expressed in the A reference frame can be written as:

$$S_r^A \vec{F} = \begin{bmatrix} 0 & -r_z & r_y \\ r_z & 0 & -r_x \\ -r_y & r_x & 0 \end{bmatrix} \begin{Bmatrix} F_x \\ F_y \\ F_z \end{Bmatrix} \tag{6}$$

Forces appearing in Eq. (4) have contributions from weight, aerodynamic loads on the canopy and payload, and apparent mass. Weights contribution is given below in Eq. (7).

$$\vec{F}_W = mg \begin{Bmatrix} -s_\theta \\ s_\phi c_\theta \\ c_\phi c_\theta \end{Bmatrix} \tag{7}$$

Aerodynamic forces on the canopy appearing in Eq. (4) are expressed in the body reference frame; however they are a function of the aerodynamics velocities in the canopy frame. Defining T_{BC} as the single axis transformation from the body to canopy reference frame by the incidence angle Γ the aerodynamic velocity of the parafoil in the canopy frame is given in Eq. (8).

$$\begin{Bmatrix} \tilde{u} \\ \tilde{v} \\ \tilde{w} \end{Bmatrix} = [T_{BC}] \left(\begin{Bmatrix} u \\ v \\ w \end{Bmatrix} + S_\omega^B \left(\begin{Bmatrix} \Delta x_c \\ \Delta y_c \\ \Delta z_c \end{Bmatrix} + [T_{BC}]^T \begin{Bmatrix} \Delta x_p \\ \Delta y_p \\ \Delta z_p \end{Bmatrix} \right) - [T_{IB}] \vec{V}_{A/I} \right) \tag{8}$$

The aerodynamic angles then become $\alpha = \operatorname{atan}(\tilde{w}/\tilde{u})$ and $\beta = \operatorname{asin}(\tilde{v}/V_A)$. Equation (9) defines the canopy aerodynamic forces in the body reference frame using T_{AC} as the transformation from aerodynamic to canopy frames by the angle α. Payload drag is defined in a similar manner in Eq. (10), where u_{SA}, v_{SA} and w_{SA} are payload aerodynamic velocities in the body frame.

$$\vec{F}_A = \frac{1}{2} \rho V_A^2 S_P [T_{BC}]^T [T_{AC}] \begin{Bmatrix} C_{D0} + C_{D\alpha 2} \alpha^2 \\ C_{Y\beta} \beta \\ C_{L0} + C_{L\alpha} \alpha + C_{L\alpha 3} \alpha^3 \end{Bmatrix} \tag{9}$$

$$\vec{F}_S = -\frac{1}{2} \rho V_S S_S C_{DS} \begin{Bmatrix} u_{SA} \\ v_{SA} \\ w_{SA} \end{Bmatrix} \tag{10}$$

Moments appearing in Eq. (5) have contributions from aerodynamic moments, apparent inertia, and from forces on the canopy and payload. Aerodynamic moments expressed in the body frame are given in Eq. (11).

$$\vec{M}_A = \frac{1}{2} \rho V_A^2 S_P [T_{BC}]^T \begin{Bmatrix} b\left(C_{l\beta}\beta + (b/2V_A)C_{lp}\tilde{p} + (b/2V_A)C_{lr}\tilde{r}\right) + C_{l\delta a}\left(\delta_a/\overline{d}\right) \\ \overline{c}\left(C_{m0} + (\overline{c}/2V_A)C_{mq}\tilde{q}\right) \\ b\left(C_{n\beta}\beta + (b/2V_A)C_{np}\tilde{p} + (b/2V_A)C_{nr}\tilde{r}\right) + C_{n\delta a}\left(\delta_a/\overline{d}\right) \end{Bmatrix} \tag{11}$$

A body moving in a fluid places the fluid in motion. The result from accelerating the fluid is a rate of change in both its linear and angular momentum. Typical aircraft having large mass to volume ratios have negligible effects from the mass of the accelerating fluid. Parafoils with small mass to volume ratios can experience large forces and moments from accelerating fluid called "apparent mass" and "apparent inertia" because they appear as additional mass and inertia values in the final equations of motion provided that their effects are not already covered by the aerodynamic coefficients. Kinetic energy of the fluid can be written as

$$2\mathrm{T} = \mathrm{A}\tilde{u}^2 + \mathrm{B}\tilde{v}^2 + \mathrm{C}\tilde{w}^2 + \mathrm{P}\tilde{p}^2 + \mathrm{Q}\tilde{q}^2 + \mathrm{R}\tilde{r}^2 + 2\mathrm{H}\left(\tilde{u}\tilde{q} + \tilde{v}\tilde{p}\right) \tag{12}$$

where it is assumed the canopy has two planes of symmetry, x-z and y-z. Asymmetry about the x-y plane is allowed to account for spanwise camber and the seven constants are defined by Lamb.[15] A canopy of general shape may have has many as 21 constants defining the kinetic energy however. Typical parafoil canopies will have approximately two planes of symmetry reducing to only seven constants. If spanwise camber is neglected the canopy can be approximated by an ellipsoid so that H becomes zero. The constants in Eq. (12) can be calculated numerically for a known shape or can be approximated as discussed in Refs. 15-17. Forces and moments from apparent mass and inertia are found by relating the fluids momentum to its kinetic energy in a similar way as Lissman and Brown[16] and are summarized in Eqs. (13) to (17). In the apparent mass contributions it is assumed that the incidence angle is slowly varying so that its derivative is negligible compared to the body angular rates.

$$\bar{F}_{AM} = -[T_{BC}]^T \left([I_{AM}] \begin{Bmatrix} \dot{\tilde{u}} \\ \dot{\tilde{v}} \\ \dot{\tilde{w}} \end{Bmatrix} + [I_H] \begin{Bmatrix} \dot{\tilde{p}} \\ \dot{\tilde{q}} \\ \dot{\tilde{r}} \end{Bmatrix} + S_\omega^C [I_{AM}] \begin{Bmatrix} \tilde{u} \\ \tilde{v} \\ \tilde{w} \end{Bmatrix} + S_\omega^C [I_H] \begin{Bmatrix} \tilde{p} \\ \tilde{q} \\ \tilde{r} \end{Bmatrix} \right) \tag{13}$$

$$\bar{M}_{AM} = -[T_{BC}]^T \left([I_H] \begin{Bmatrix} \dot{\tilde{u}} \\ \dot{\tilde{v}} \\ \dot{\tilde{w}} \end{Bmatrix} + [I_{AI}] \begin{Bmatrix} \dot{\tilde{p}} \\ \dot{\tilde{q}} \\ \dot{\tilde{r}} \end{Bmatrix} + S_\omega^C [I_H] \begin{Bmatrix} \tilde{u} \\ \tilde{v} \\ \tilde{w} \end{Bmatrix} + S_\omega^C [I_{AI}] + S_{V_A}^C [I_H] \begin{Bmatrix} \tilde{p} \\ \tilde{q} \\ \tilde{r} \end{Bmatrix} \right) \tag{14}$$

$$[I_{AM}] = \begin{bmatrix} \mathrm{A} & 0 & 0 \\ 0 & \mathrm{B} & 0 \\ 0 & 0 & \mathrm{C} \end{bmatrix} \tag{15}$$

$$[I_{AI}] = \begin{bmatrix} \mathrm{P} & 0 & 0 \\ 0 & \mathrm{Q} & 0 \\ 0 & 0 & \mathrm{R} \end{bmatrix} \tag{16}$$

$$[I_H] = \begin{bmatrix} 0 & \mathrm{H} & 0 \\ \mathrm{H} & 0 & 0 \\ 0 & 0 & 0 \end{bmatrix} \tag{17}$$

Notice the forces and moments from apparent mass are a function of the canopy incidence angle. Equations (13) and (14) couple the linear and rotational dynamic in Eqs. (4) and (5). Final dynamic equations of motion are found by substituting all forces and moments into Eqs. (4) and (5) resulting in the matrix solution shown in Eqs. (18) and (20). The common convention is used for tensors of second rank such that $[I_X'] = [T_{BC}]^T [I_X][T_{BC}]$ for the quantities in Eqs. (15) to (17).

$$\begin{bmatrix} m\mathrm{I} + [I'_{AM}] & [I'_H] - [I'_{AM}] S_{CG,M}^B \\ S_{CG,M}^B [I'_{AM}] + [I'_H] & I_T + [I'_{AI}] - [I'_H] S_{CG,M}^B + S_{CG,M}^B ([I'_H] - [I'_{AM}]) S_{CG,M}^B \end{bmatrix} \begin{Bmatrix} \dot{u} \\ \dot{v} \\ \dot{w} \\ \cdots \\ \dot{p} \\ \dot{q} \\ \dot{r} \end{Bmatrix} = \begin{Bmatrix} \Phi \\ \cdots \\ \mathrm{M} \end{Bmatrix} \tag{18}$$

$$\Phi = \vec{F}_A + \vec{F}_s + \vec{F}_W - mS_\omega^B \begin{Bmatrix} u \\ v \\ w \end{Bmatrix} - [T_{BC}]^T S_\omega^C \left([I_{AM}] \begin{Bmatrix} \tilde{u} \\ \tilde{v} \\ \tilde{w} \end{Bmatrix} + [I_H] \begin{Bmatrix} \tilde{p} \\ \tilde{q} \\ \tilde{r} \end{Bmatrix} \right) - [I'_{AM}] S_\omega^B [T_{IB}] \vec{V}_{A/I} \qquad (19)$$

$$M = \vec{M}_A + S_{CG,P}^B \vec{F}_A + S_{CG,S}^B \vec{F}_S - S_\omega^B [I_T] \begin{Bmatrix} p \\ q \\ r \end{Bmatrix} - S_{CG,M}^B [T_{BC}]^T S_\omega^C \left([I_{AM}] \begin{Bmatrix} \tilde{u} \\ \tilde{v} \\ \tilde{w} \end{Bmatrix} + [I_H] \begin{Bmatrix} \tilde{p} \\ \tilde{q} \\ \tilde{r} \end{Bmatrix} \right)$$

$$- [T_{BC}]^T S_\omega^C [I_H] \begin{Bmatrix} \tilde{u} \\ \tilde{v} \\ \tilde{w} \end{Bmatrix} + [T_{BC}]^T \left(S_\omega^C [I_{AI}] + S_{V_{A/I}}^C [I_H] \right) \begin{Bmatrix} \tilde{p} \\ \tilde{q} \\ \tilde{r} \end{Bmatrix} - \left(S_{CG,M}^B [I'_{AM}] + [I'_H] \right) S_\omega^B [T_{IB}] \vec{V}_{A/I} \qquad (20)$$

The matrix in Eq. (18) appears as an inertia matrix and satisfies many properties of a typical inertia matrix such as symmetry. In the case where all apparent mass and inertia effects are negligible Eq. (18) reduces to a block diagonal system where linear and rotational dynamic equations decouple. The effective apparent mass and inertia matrices I'_{AM}, I'_H and I'_{AI} are functions of the canopy incidence angle so that changing the incidence angle for glide slope control results in varying apparent mass and inertia matrices. This is in contrast to conventional models where apparent mass and inertia coefficients are assumed constant.

IV. Flight Testing

The parafoil system tested is shown in Figs. 6 and 7 with the canopy deployed and undeployed, respectively. The payload of the system consists of a 6 in × 6 in × 18 in cardboard box with two avionic boxes on either end. The upper avionics box, consists of a data logger with battery, canopy pack, and a Hitec HS-311 servo used to release the packed parafoil. Sensors included in the upper avionics are three accelerometers, gyroscopes and magnetometers, a global positioning system and barometric altimeter. The upper box was designed to allow the top flaps of the cardboard box to flare out at a 45 deg angle to allow the undeployed system to be cone stabilized (see Fig. 7). The lower avionics box contains three Hitec HS-785 HB sail winches, a Hitec Electron 6 FM receiver, and a battery pack. Sail winch 1 and 2 control the right and left brake lines, while sail winch 3 controls the front lines of the parafoil. The sail winch signals are mixed together so that as the front lines are pulled in, the brake lines are let out and vise versa. This allows the geometry of the canopy to accommodate for different incidence angles. Note the rear lines of the canopy remain fixed to the upper box while the brake lines and front lines run through the upper avionics box, to the sail winches in the lower avionics box.
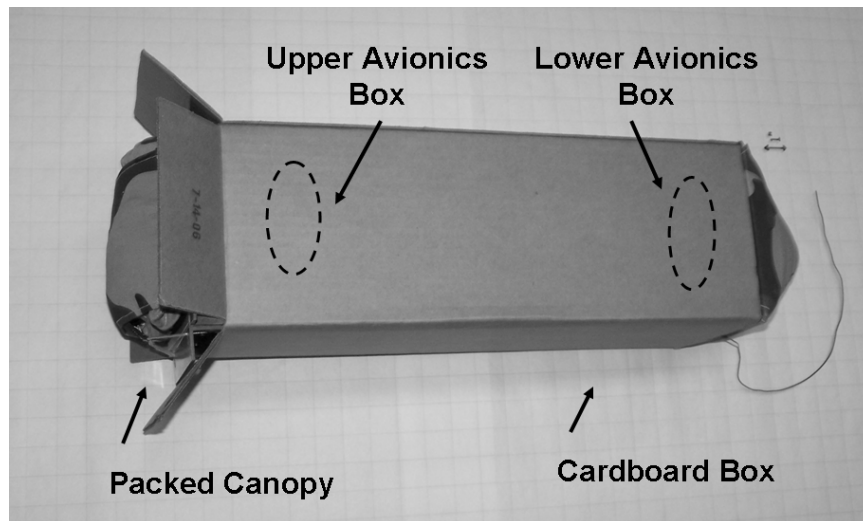
Fig. 6 Test System with Deployed Parafoil

Fig. 7   Test System with Undeployed Parafoil

As mentioned above; the incidence angle of the parafoil is changed using the three sail winches in the lower avionics box. An example of this incidence change is shown in Fig. 8. Two different parafoil systems were used in this study. Systems 1 and 2 differ mainly in their canopy thickness, leading edge geometry and payload weight. The dimensions of the systems are shown in Fig. 9 and outlined in Table 1.
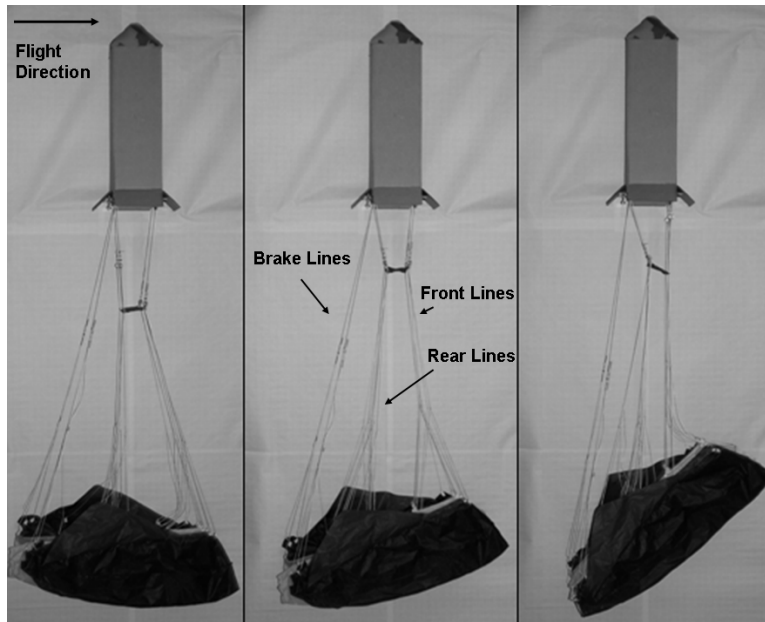
American Institute of Aeronautics and Astronautics

Fig. 4   Parafoil Incidence Angle Change

θ_1

h

SIDE VIEW

b

c

TOP VIEW

θ_2

FRONT VIEW
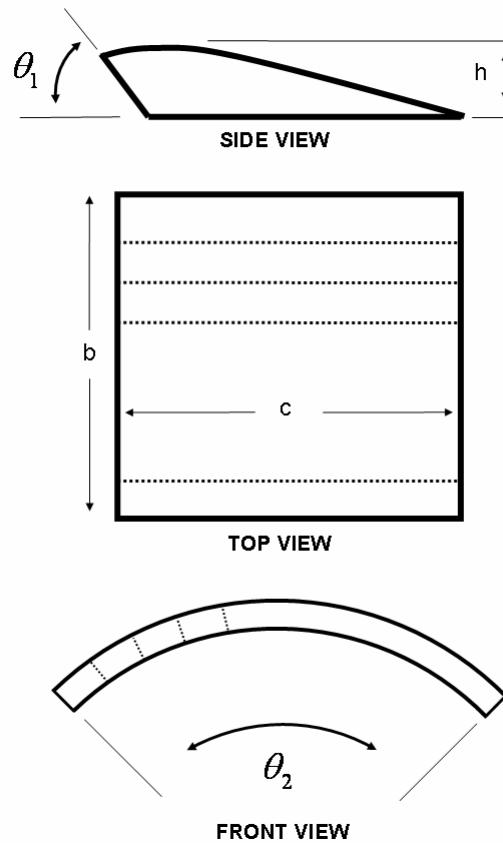
Fig. 5   Canopy Geometry

Table 1   System Characteristics

Parameter	System 1	System 2
θ_1 (deg)	80	50

θ_2 (deg)	45	45
h (ft)	0.35	0.17
b (ft)	4.5	5.0
c (ft)	2.1	1.3
Weight(lbf)	5.23	1.59

Four flight tests were conducted in low wind conditions, two for each system. System 1 was configured with a nominal incidence Γ_1 of -6 deg and once equilibrium was achieved the incidence angle was changed. In the first flight of System 1 the canopy was rotated down to an incidence Γ_2 of -24 deg, while during the second flight the canopy was rotated up to an incidence Γ_3 of 10 deg. System 2 was configured with a nominal incidence Γ_4 of -24 deg and was subsequently rotated down to an incidence Γ_5 of -44 deg for both the third and fourth flight tests. Results are shown after canopy opening in Figs. 10 to 12. Figure 14 shows results for the flight path where both altitude and distance have been non-dimensionalized with respect to the initial altitude. The flight path angle λ can be seen by the slope of the flight path in Fig. 10 and the glide slope (GS) is defined as $-1/\tan(\lambda)$. Table 2 summarizes the four flight tests.
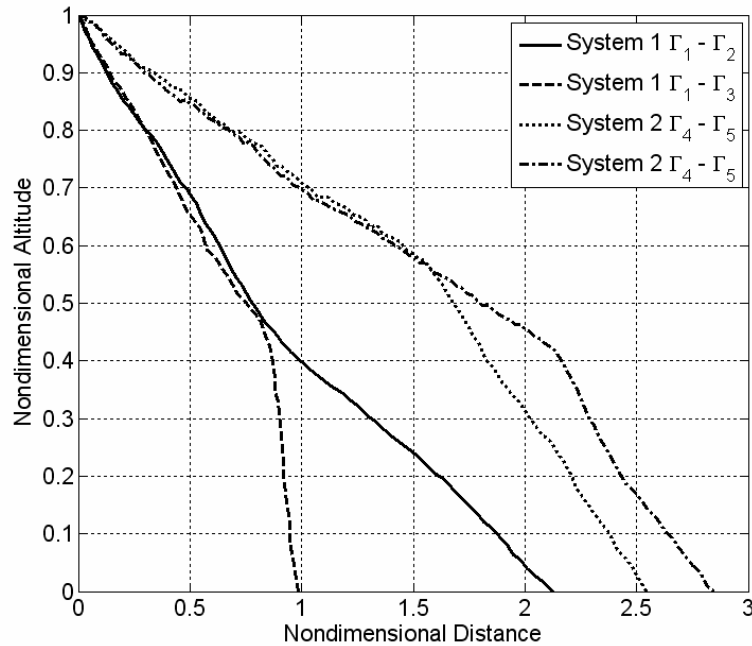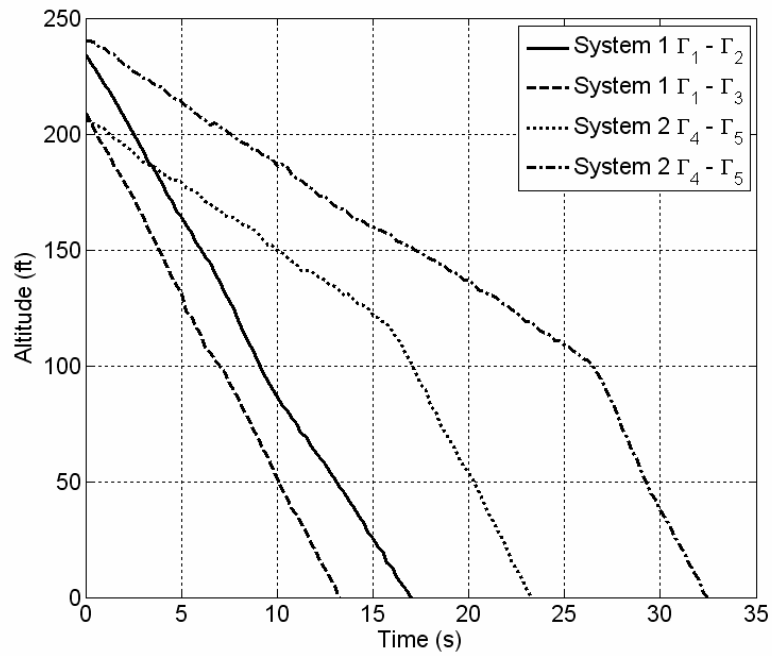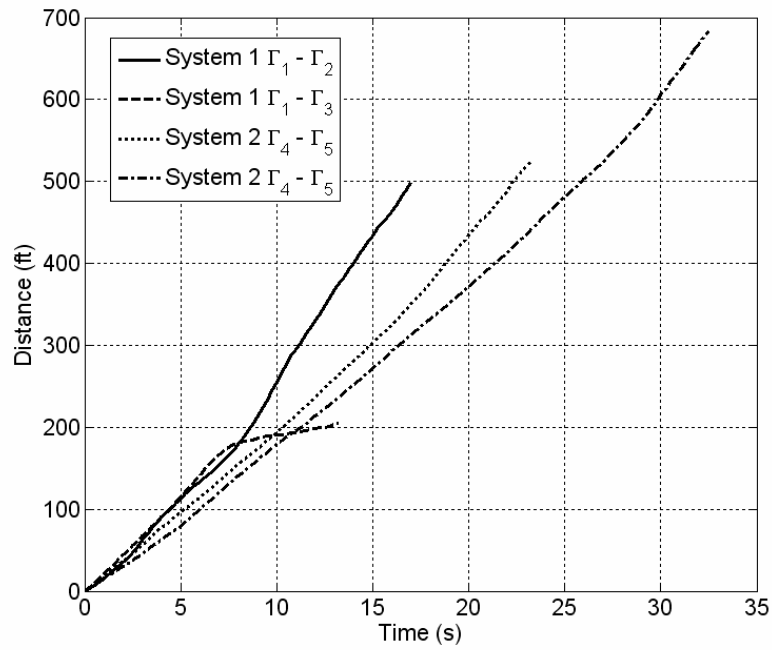

Fig. 10 Flight Path Angle

Fig. 11 Altitude

Fig. 12 Distance Traveled

Table 2   Flight Test Summary

	System 1 Γ_1 = -6 deg	System 1 Γ_2 = -24 deg	System 1 Γ_3 = 10 deg	System 2 Γ_4 = -24 deg	System 2 Γ_5 = -44 deg
α (deg)	28	6	70	10	5
Glide Slope	1.45	2.46	0.28	3.70	1.94

Speed (ft/s)	26	35	16	21	26
C_L	0.56	0.35	0.49	0.45	0.27

System 1 responds to a decrease in incidence from -6 to -24 deg with a 70 percent increases in GS, from 1.45 to 2.46. Increasing the incidence from -6 to 10 deg results in a stalled condition where the GS is decreased 89 percent. System 2 responds in an opposite manner with a decrease in incidence from -24 to -44 deg resulting in a 48 percent decrease in GS from 3.70 to 1.94. Differences are also observed in the vertical and forward velocity trends where for System 1 changing the incidence results in large forward speed changes with vertical speed remaining nearly unchanged while for System 2 the opposite is true. Results from System 1 were used to estimate C_L and C_D curves for the combined system including payload. The C_L and C_D curves are approximated by a cubic and quadratic curves defined by C_{L0}, $C_{L\alpha}$, $C_{L\alpha 3}$, C_{D0}, and $C_{D\alpha 2}$. Using results for System 1 in Table 2 the coefficients are estimated as 0.28, 0.68, -0.35, 0.135, and 0.95 respectively. Figure 13 shows the estimated curves compared with the measured results for System 1 including canopy and payload. The estimated values are consistent with results from Ware and Hassell[2] who observed maximum lift to drag ratios near 2.5, high profile drag and low maximum lift coefficients when compared to a standard rigid wing. It is important to note that as demonstrated by results from Ware and Hassell[2] the C_L curve is typically flat near stall with the exact angle of attack at stall difficult to define. The C_L curve is approximated well by a cubic function prior to and post stall however a higher order function is required to approximate the stall region. The estimated C_L curve in Fig. 13 is valid at angles of attack lower than 30 deg and higher than 70, the location of the maximum C_L can only be identified as occurring within that. Estimation of the stall region is unnecessary because all glide slope control and simulations occur prior to this region. Simulations of the estimated system GS are shown in Fig. 14 and are consistent with test data.
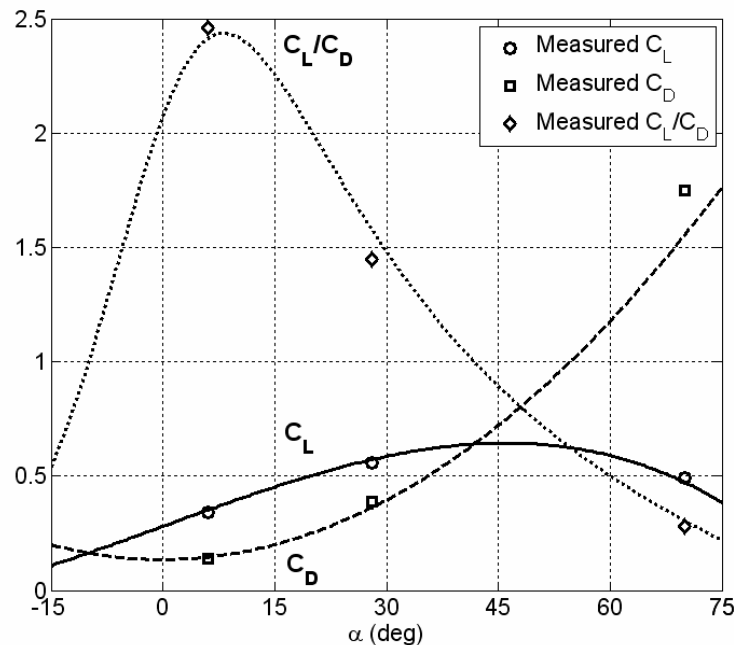

Fig. 13 Estimated Lift Coefficient, Drag Coefficient, and C_L/C_D for System 1including payload
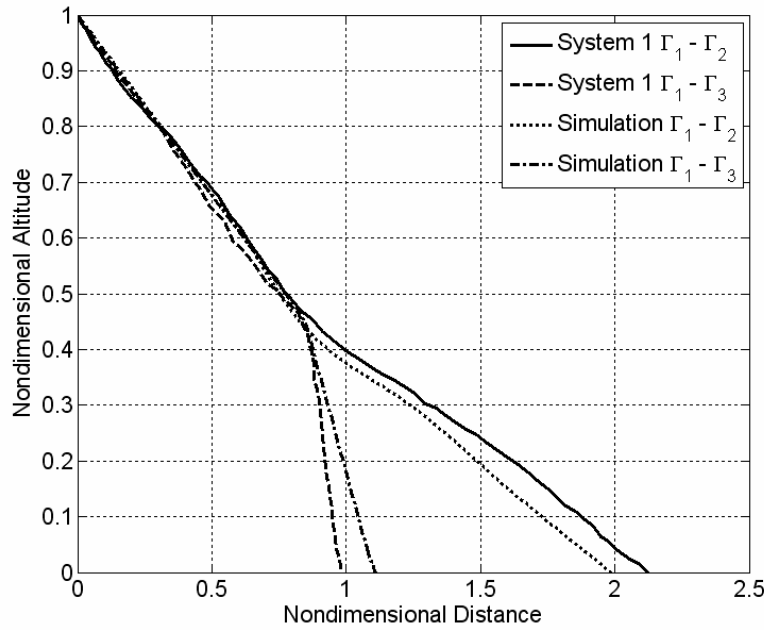
Fig. 14 Comparison of Simulated and Measured GS for System 1

From Fig. 13 System 1 operates to the right of its maximum lift to drag ratio for all incidence angles resulting in an increased GS as the incidence is decreased. Decreasing the incidence of System 2 resulted in a decreased GS demonstrating System 2 operates to the left of its maximum lift to drag ratio. Noting that the maximum L/D occurs well before stall, its angle of attack can be estimated using Eq. (21).

$$\alpha_{L/D\ MAX} = \sqrt{\left(\frac{C_{L0}}{C_{L\alpha}}\right)^2 + \frac{C_{D0}}{C_{D\alpha2}}} - \frac{C_{L0}}{C_{L\alpha}} \qquad (21)$$

Equation 21 shows the maximum L/D angle of attack increases as $C_{L\alpha}$ increases and $C_{D\alpha2}$ decreases, both occurring as the lifting surface efficiency factor increases. This is consistent with System 2 having a small thickness to chord ratio, larger aspect ratio and more rounded nose. Parafoils of higher efficiency will be able to operate to the left of their maximum L/D, while an inefficient canopy may operate to the right. It is demonstrated by Systems 1 and 2 that a parafoil system can effectively operate on either side of the maximum L/D angle of attack and have effective glide slope control. A system however may be arranged such that it operates near its maximum L/D, in such a case minimal glide slope control will result from the small slope of the L/D curve in this vicinity.

Simulations were completed for System 1 where the incidence was decreased from -6 to -12, -18 and -24 deg at 15 second intervals with each changes occurring linearly over a second. Figure 19 shows the glide slope dynamics persist for 5 seconds after each change in incidence. The GS initially decreases in response to the decreased lift from decreasing angle of attack before it increases as the speed increases. Changes in angle of attack and velocities are shown in Figs. 16 and 17, respectively. As incidence is decreased the angle of attack decreases approaching the maximum L/D where GS control authority diminishes. A nearly linear GS mechanism can be implemented for System 1 by designing the nominal incidence to be -12 deg so that ±25% changes in GS can be achieved over a -6 to -18 incidence range. If maximum L/D flight is desired System 1 can be flown at an incidence of -18 deg, however, the GS can only be effectively decreased.
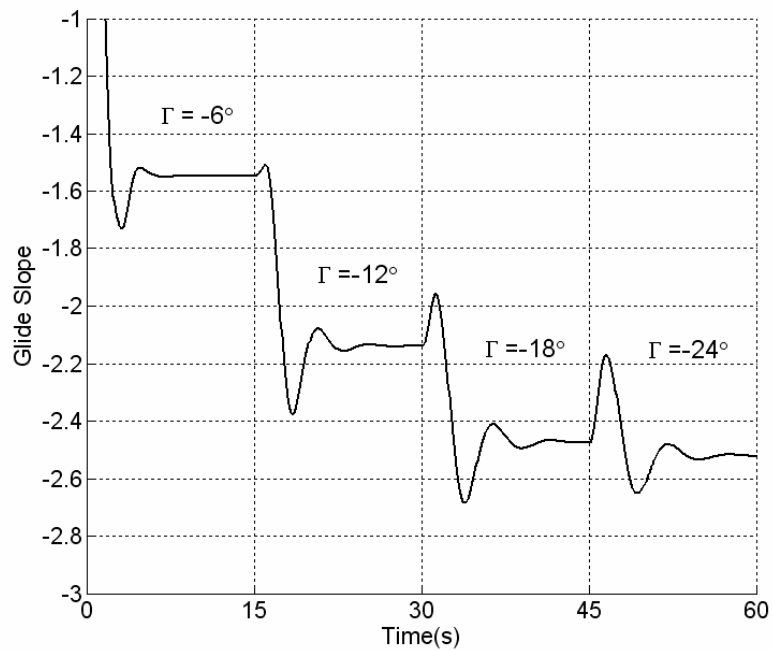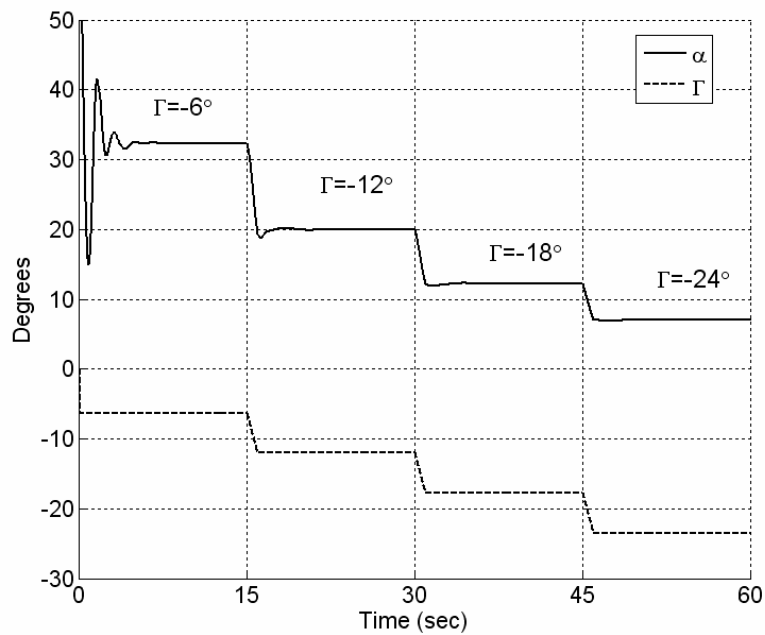
Fig. 15   Simulated GS Varying Incidence Γ of System 1

Figure 16. Simulated Angle of Attack Varying Incidence Γ of System 1

17
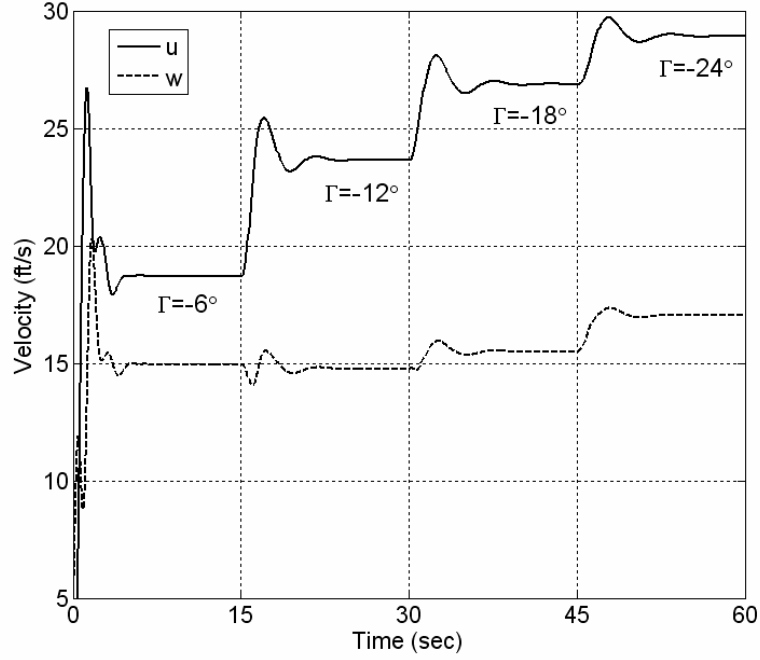American Institute of Aeronautics and Astronautics

Fig. 17   Simulated Velocities Varying Incidence Γ of System 1

V. Precision Placement Simulation

The precision placement trajectory tracking algorithm used here is based on a Model Predictive Control (MPC) scheme that tracks desired heading and was successfully demonstrated on a small parafoil by Slegers and Costello.[18] It was also shown in Ref 18 that linearization of a parafoil model results in the lateral dynamics being decoupled form longitudinal dynamics. Consider a SISO linear discrete system described in state space form as given in Eq. (22).

$$x_{k+1} = Ax_k + Bu_k$$
$$y_k = Cx_k \tag{22}$$

Assume the system matrices A, B and C are known and that x_k is the state vector $\begin{bmatrix} \phi_k & \psi_k & p_k & r_k \end{bmatrix}^T$, u_k is the asymmetric brake deflection δ_a , and y_k is the output ψ_k at time k . The model described above can be used to estimate the future state of the system. Assuming a desired trajectory is known an estimated error signal $\tilde{e}_k = w_k - \tilde{y}_k$ is computed over a finite set of future time instants called the prediction horizon, H_p , where w_k is the desired output and the symbol ~ is used to represent an estimated quantity. In model predictive control, the control computation problem is cast as a finite time discrete optimal control problem. To compute the control input at a given time instant, a quadratic cost function is minimized through the selection of the control history over the control horizon. The cost function can be written as:

$$J = \left(W - \tilde{Y}\right)^T \left(W - \tilde{Y}\right) + U^T R U \tag{23}$$

where,

$$W = \begin{Bmatrix} w_{k+1} & w_{k+2} & \cdots & w_{k+H_p} \end{Bmatrix}^T \tag{24}$$

$$\tilde{Y} = K_{CA} x_k + K_{CAB} U \tag{25}$$

$$U = \left\{ u_k \quad u_k \quad \cdots \quad u_{k+H_p-1} \right\}^T \tag{26}$$

and R is a symmetric positive semi-definite weighting matrix penalizing control having size H_p. Equation 25 is used to express the predicted output vector $\widetilde{Y}$ in terms of the system matrices.

$$K_{CA} = \begin{bmatrix} CA \\ CA^2 \\ \vdots \\ CA^{HP} \end{bmatrix} \tag{27}$$

$$K_{CAB} = \begin{bmatrix} CB & 0 & 0 & 0 & 0 \\ CAB & CB & 0 & 0 & 0 \\ CA^2B & CAB & CB & 0 & 0 \\ \vdots & \vdots & & \ddots & 0 \\ CA^{H_p-1}B & \cdots & CA^2B & CAB & CB \end{bmatrix} \tag{28}$$

Equations 25 and 26 can be substituted into the cost function of Eq. (23) resulting in Eq. (29) that is in terms of the system state x_k, desired trajectory W, control vector U and system matrices A, B, C, and R.

$$J = \left(W - K_{CA}x_k - K_{CAB}U \right)^T \left(W - K_{CA}x_k - K_{CAB}U \right) + U^T RU \tag{29}$$

The control U, which minimizes Eq. (29) is

$$U = \mathrm{K}\left(W - K_{CA}x_k \right) \tag{30}$$

where,

$$\mathrm{K} = \left(K_{CAB}{}^T K_{CAB} + R \right)^{-1} K_{CAB}{}^T \tag{31}$$

Equation 30 contains the optimal control inputs over the entire control horizon, however at time k only the first element u_k is needed. The first element u_k can be extracted from Eq. (30) by defining K_1 as the first row of K. The optimal control over the next time sample becomes were a description of estimating the desired heading for a parafoil is provided in Ref. 18.

$$u_k = \mathrm{K}_1\left(W - K_{CA}x_k \right) \tag{32}$$

Glide slope control is treated separately from heading tracking and is implemented similar to proportional navigation of guided missiles. A diagram of the glide slope guidance is shown in Fig. 14 where r_{LOS} is the line of sight vector from the parafoil to the target. As the parafoil approaches the target any misalignment of the velocity vector and r_{LOS} will result in r_{LOS} rotating with the angular velocity ω_{LOS} provided in Eqn. 33. In order for the parafoil to impact the target the angular velocity of the line of sight vector ω_{LOS} must be zero, if the parafoil is falling too fast or too slow ω_{LOS} will be positive or negative, respectively. A Proportional-Integral controller using incidence angle as control is implemented to track zero ω_{LOS}, thus placing the system on the required GS to impact the target.

$$\omega_{LOS} = \frac{V}{D}\sin\left(\theta_{LOS} + \lambda\right) \tag{33}$$
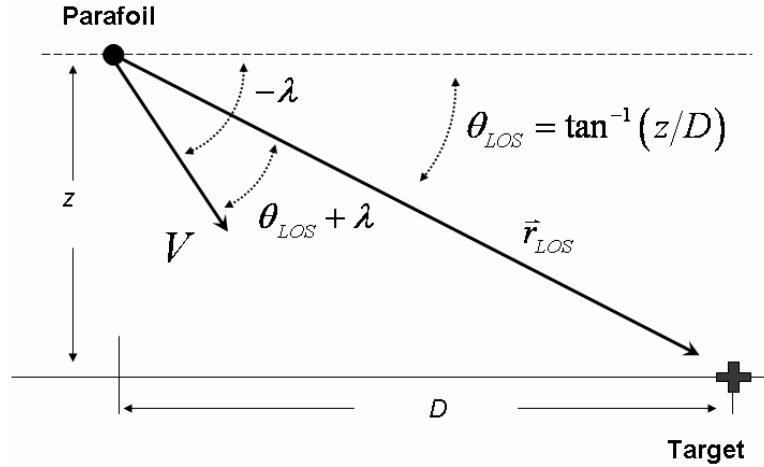
Fig. 18   Glide Slope Guidance Geometry

The MPC algorithm requires a desired heading trajectory which is defined by four parameters: Target Location, Away Distance, Cycle Distance and Wind Heading Angle. As shown in Fig. 19, these four parameters define three fixed tracking points: Target Point, Away Point and Cycle Point. Using these three points, precision placement objectives are divided into four phases when glide slope control is implemented and five phases otherwise. The phases are pictured in Fig. 19 and defined as follows:

Phase1:   The system is released up wind to ensure it reaches the target in strong winds. System travels a direct path to the Cycle Point.

Phase 2:   System circles around the Away and Cycle Point. Down wind glide slope is estimated when traveling toward the Target Point. This continues until the Switch Altitude is reached. The Switch Altitude is defined as the distance to the target divided by the estimated glide slope plus an excess altitude. Excess altitude is only required when glide slope control is absent. Excess altitude allows the system to turn to the target early because when GS control is absent the effective GS cannot be increased only reduced by swerving.

Phase 3:   System travels directly to the Away Point. Glide slope estimation is terminated.

Phase 4:   No GS Control - System continues glide slope estimation. At each update time the distance to the target and a distance to waste are calculated. MPC turns left and right tracking an "S" trajectory generated by waypoints to waste an appropriate distance to impact the target.

GS Control - At each update time the angular velocity ω_{LOS} of the line of sight vector is calculated and a proportional-integral controller regulates it to zero. MPC tracks a path directly to the target.

Phase 5:   The system flies directly to the target once a Critical Altitude is achieved.
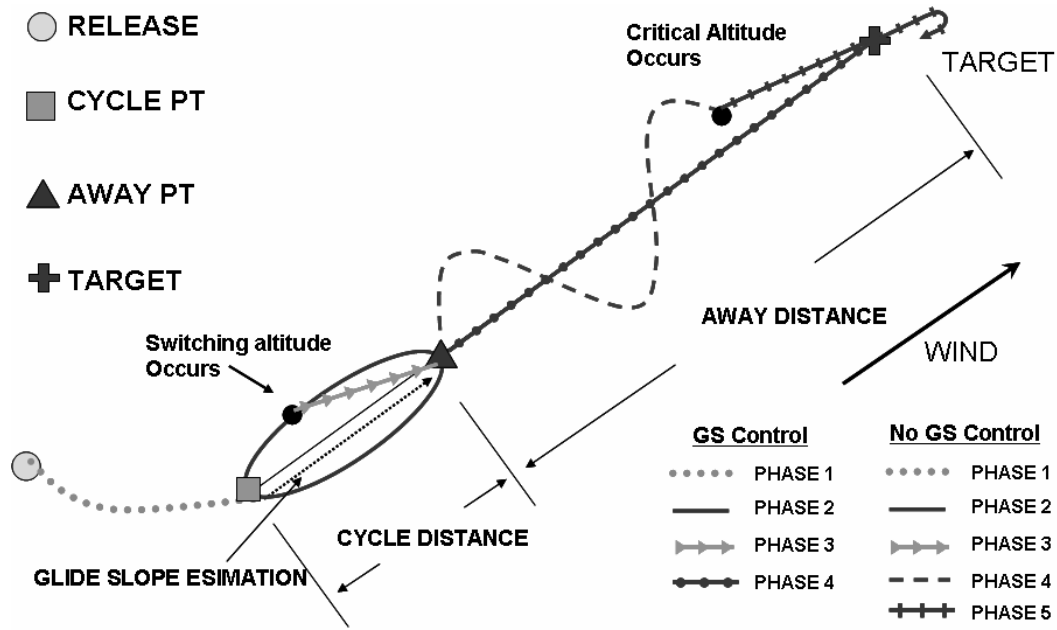
Fig. 19   Phases of Precision Placement Algorithm

Nominal simulations of the precision placement algorithm with MPC were performed for the canopy and payload of System 1. The nominal incidence is -12 deg and physical parameters are listed in Table 3. Aerodynamic coefficients listed in Table 3 were estimated from dynamic maneuvers during flight testing. The discrete linear matrices used for MPC are provided in Eqs. (34) and (35) where the discretization period is 0.5 seconds. The system is released from an altitude of 2500 ft, 2500 ft down range and 150 ft cross range with a desired target at the origin. Away and Cycle Distance are 2000 and 1000 ft respectively. Without GS control the Critical and Excess Altitudes are 100 and 200 ft, respectively. A 5 ft/s tail wind rotated 10 deg with respect to the target line is used both with and without GS control. Results are shown in Figs. 20 through 24 where both methods impact within 15 ft of the target. Phases 1 and 2 are identical for both methods. Phase 3 is entered sooner without GS control as seen in Figs. 20 and 21 because of the required excess altitude. Phase 3 is entered at an altitude of 1250 ft at 103 sec without GS control and 1050 ft at 111 sec with GS control. Phase 4 is entered at 132 sec without GS control and at 140 sec with GS control. During phase 4 the system with GS control varies the canopy incidence and angle of attack to adjust for errors in GS as seen in Figs. 22 and 23. The system without GS control swerves left and right to adjust the effective GS requiring more active brake maneuvers in the final stages as shown in Fig. 24. An advantage of GS control is seen during the fourth phase. Over the last 2000 ft of range the system with GS control maintains a constant orientation with respect to the target and wind enabling accurate GS estimation. Swerving required by the system without GS control changes the orientation with respect to the wind. As the system faces toward positive and negative cross range the wind slows and increases the forward speed respectively. Changing speeds make accurate GS estimation more difficult while the variation in cross range induces additional errors in impact.

Table 3 Parafoil and Payload Physical Parameters

Parameter	Value	Units
I_{XX}	0.312	$slug \cdot ft^2$
I_{YY}	0.296	$slug \cdot ft^2$
I_{ZZ}	0.039	$slug \cdot ft^2$
I_{XZ}	0.022	$slug \cdot ft^2$
$C_{Y\beta}$	-0.20	-
C_{lp}	-0.15	-
$C_{l\delta a}$	–0.005	-

C_{ma}	-0.40	-
C_{nr}	-0.09	-
$C_{n\delta a}$	0.007	-
C_{DS}	0.30	-
S_S	0.65	ft^2
A	0.0008	$slug$
B	0.0022	$slug$
C	0.0290	$slug$
H	0.0014	$slug$
P	0.040	$slug \cdot ft^2$
Q	0.100	$slug \cdot ft^2$
R	0.0018	$slug \cdot ft^2$

$$A = \begin{bmatrix} 0.899 & 0 & 0.180 & 0.020 \\ 0.008 & 1.000 & 0.001 & 0.033 \\ -0.119 & 0 & -0.017 & -0.002 \\ 0.008 & 0 & 0.002 & 0.000 \end{bmatrix} \quad (34)$$

$$B = \begin{bmatrix} 0.001 \\ 0.101 \\ -0.012 \\ 0.104 \end{bmatrix} \quad (35)$$
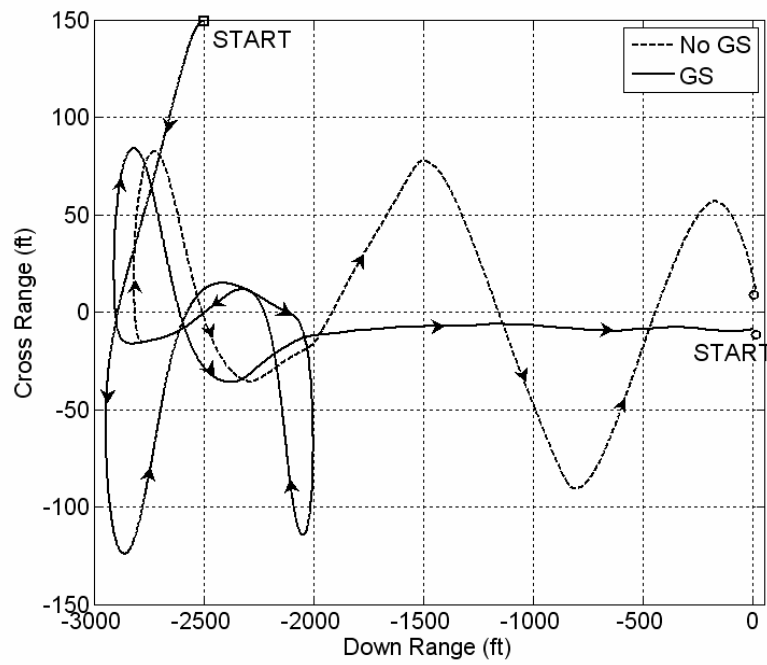
Fig. 20 Simulated Precision Placement Cross Range
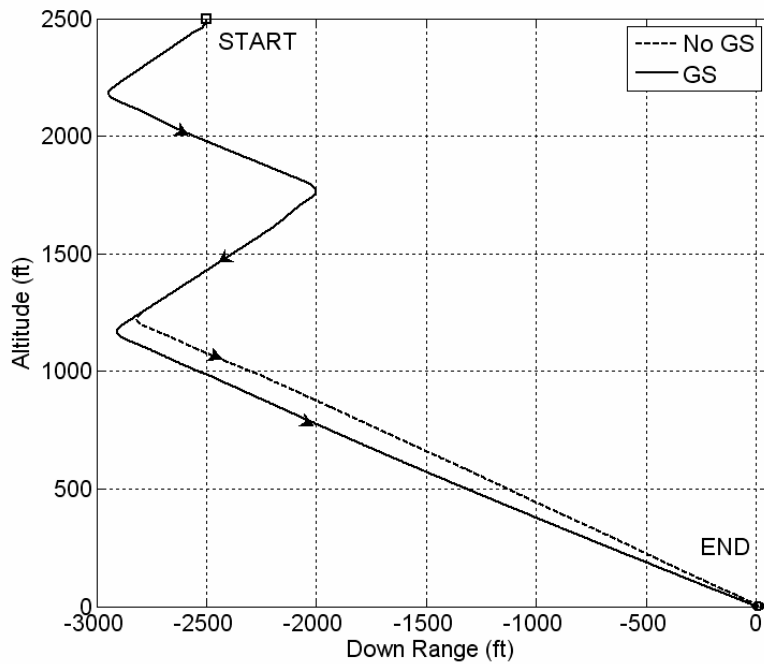
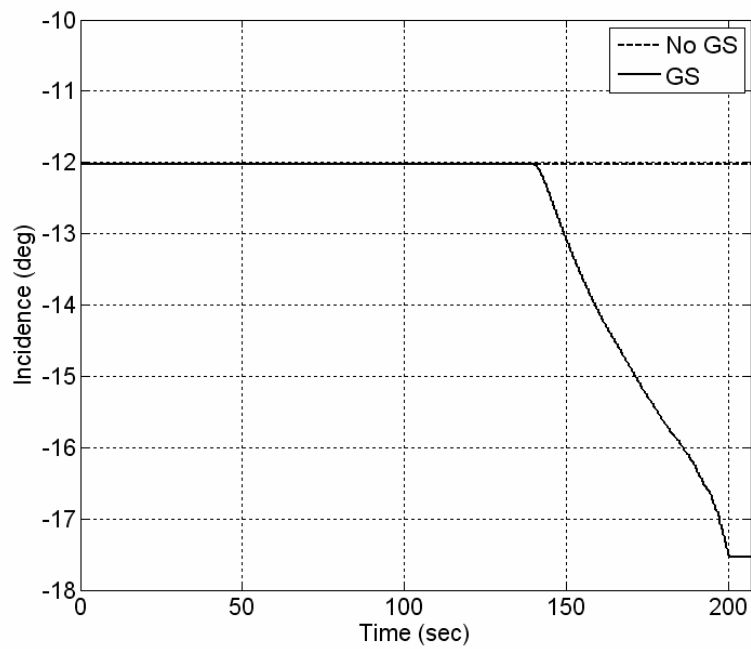Fig. 21 Simulated Precision Placement Altitude

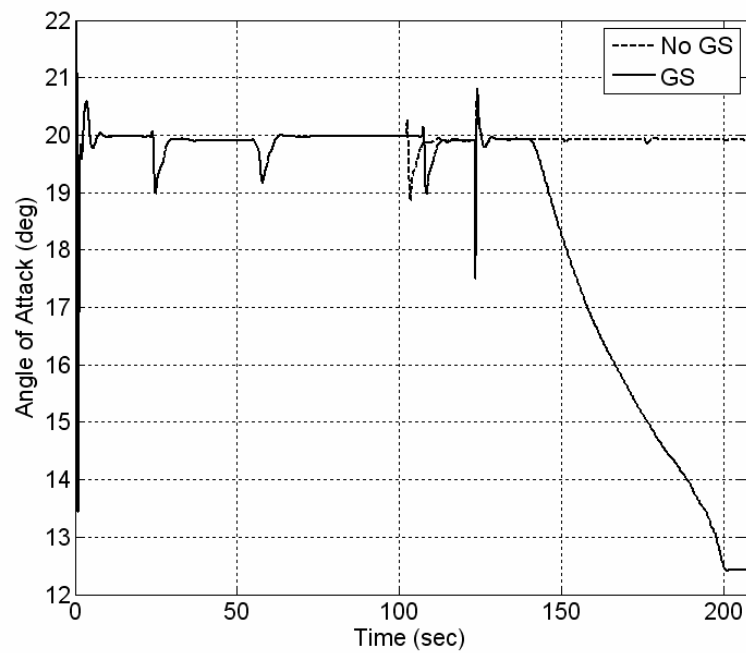Fig. 22   Simulated Precision Placement Incidence Angle

Fig. 23   Simulated Precision Placement Angle of Attack

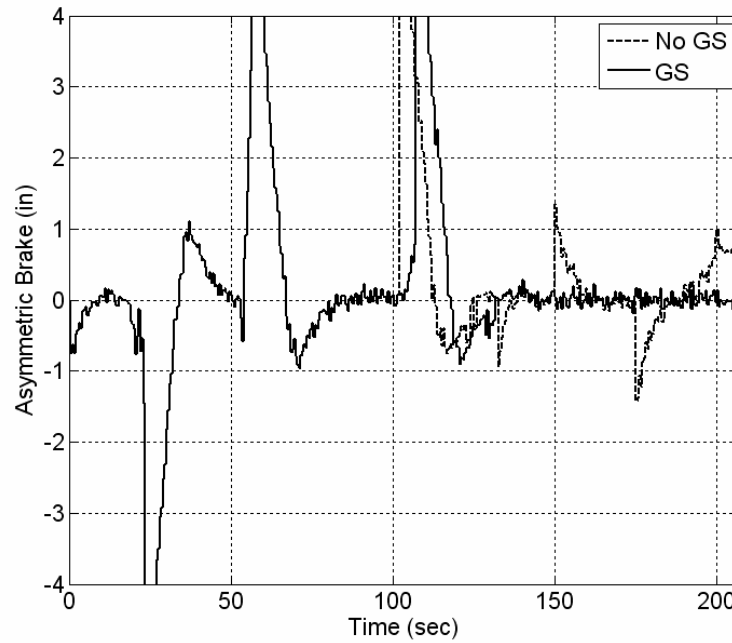American Institute of Aeronautics and Astronautics

Fig. 24   Simulated Precision Placement Asymmetric Control.

Monte Carlo simulations of 100 drops were completed using the Precision Placement Algorithm with MPC. Noise was injected into GPS, Altitude, and IMU sensors. In addition to sensor errors, three sources of wind variation were added to the simulation; wind shear, varying magnitude and direction. The wind was divided into two segments varied independently, namely, wind above 1000 ft and wind below 1000 ft in order to simulated inconsistent wind profiles. Prevailing wind was assumed by the system to come from a heading of zero degrees while true wind varied in its direction. For all simulations, the target was set as the origin. Sensor noise and wind variation statistics are listed in Table 4.

Table 4   Error Statistics

Parameter	Mean	Standard Deviation
Initial Condition Position X	3500 ft	750 ft
Initial Condition Position Y	0 ft	750 ft
Initial Condition Position Z	4500 ft	750 ft
GPS X Bias	0.0 ft	3.0 ft
GPS Y Bias	0.0 ft	3.0 ft
GPS X Deviation	1.0 ft	0.0 ft
GPS Y Deviation	1.0 ft	0.0 ft
Altitude Bias	0.0 ft	5.0 ft
Altitude Variation	1.0 ft	0.0 ft
Roll, Pitch and Yaw Bias	0.0 deg	1.7 deg
Roll, Pitch and Yaw Deviation	1.7 deg	0.0 deg
u,v and w Bias	0.0 ft/s	0.1 ft/s
u,v and w Deviation	0.7 ft/s	0.0 ft/s
p, q, and r Bias	0.0 deg	1.7 deg
p, q, and r Deviation	1.0 deg	0.0 deg
Wind1	10.0 ft/s	3.0 ft/s
Wind2	10.0 ft/s	3.0 ft/s

Wind Heading Error	0.0 deg	11.0 deg

      Monte Carlo simulations were first completed with and without GS control including sensor errors and no wind. Dispersion results are shown in Fig. 25 while histograms are provided in Figs. 26 and 27. The circular error probable (CEP) defined by the radius which includes 50 percent of the impacts are shown by a circle. CEP with and without GS control are 9.8 and 13.2 ft respectively with dispersion patterns being similar in both cases. The main difference is found in the histograms where without GS control impacts are skewed toward larger errors, where 5% of impacts have more than 30 ft of error. With GS control no impact has more than 30 ft of error.
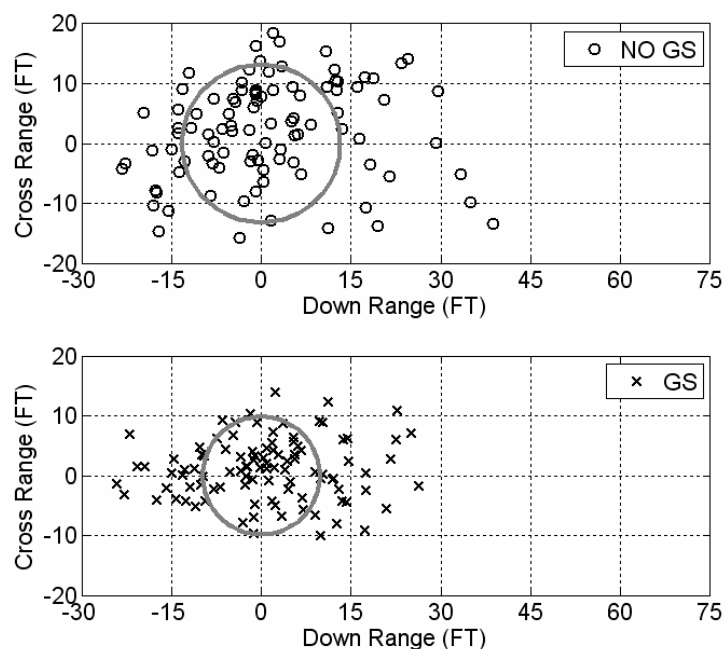

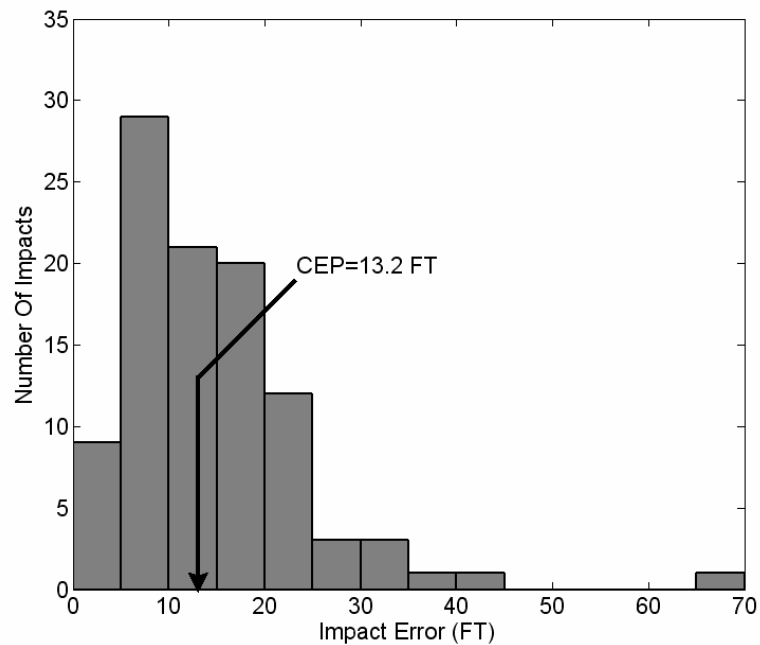Fig. 25 Dispersion for All Sensor Errors and No Wind

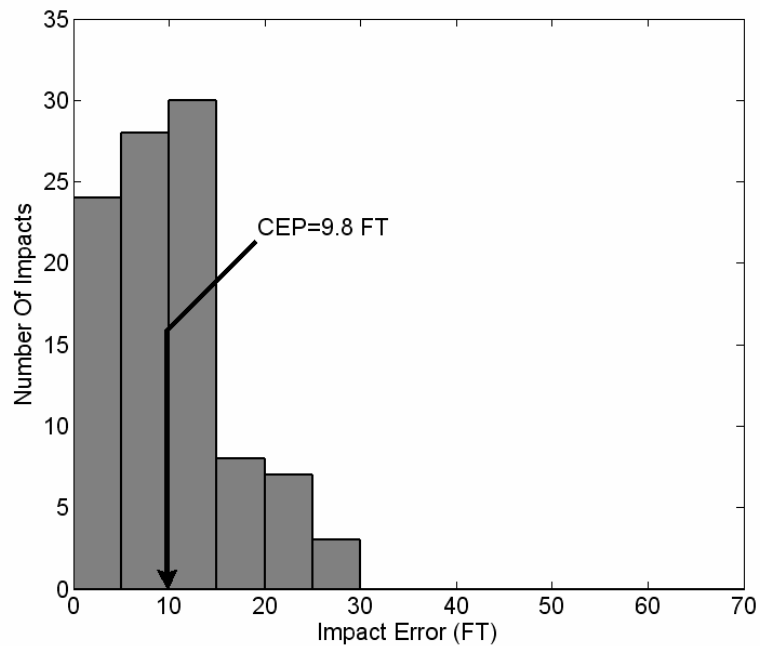Fig. 26   Without GS Control Histogram for Sensor Errors and No Wind

Fig. 27   GS Control Histogram for Sensor Errors and No Wind

Results including both sensor errors and wind variations are shown in Figs. 28 through 30. CEP with and without GS control are 16.7 and 72.4 ft respectively. Including winds, the GS control CEP increased by only 70 percent while the CEP without GS control increased 450 percent. Including GS control a reduction by more than a factor of three is achieved in CEP and sensitivity to winds is reduced. Dispersion patterns also differ significantly. With GS control the dispersion in mainly in range with 97 percent of the cases having less than 20 ft of cross range error.

American Institute of Aeronautics and Astronautics

Swerving required without GS control increased dispersion in cross range. GS control also reduced errors greater than 200 ft from 11 to 1.
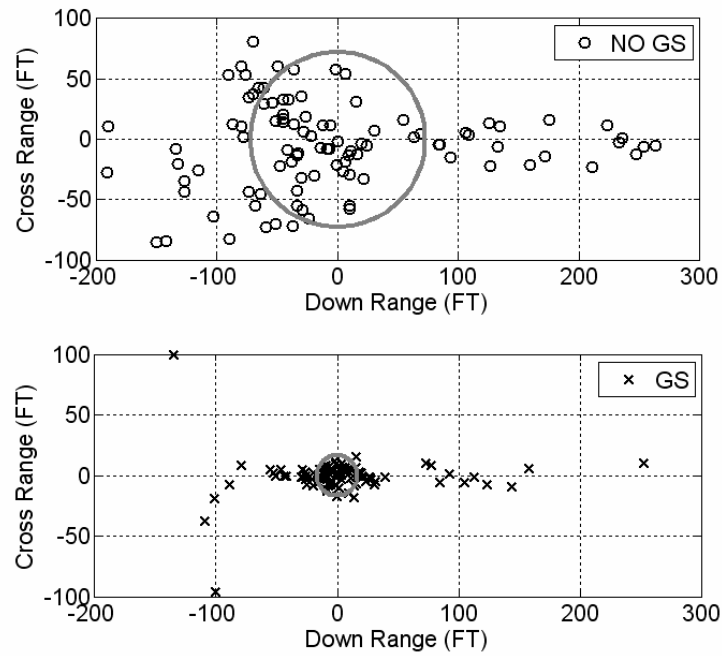

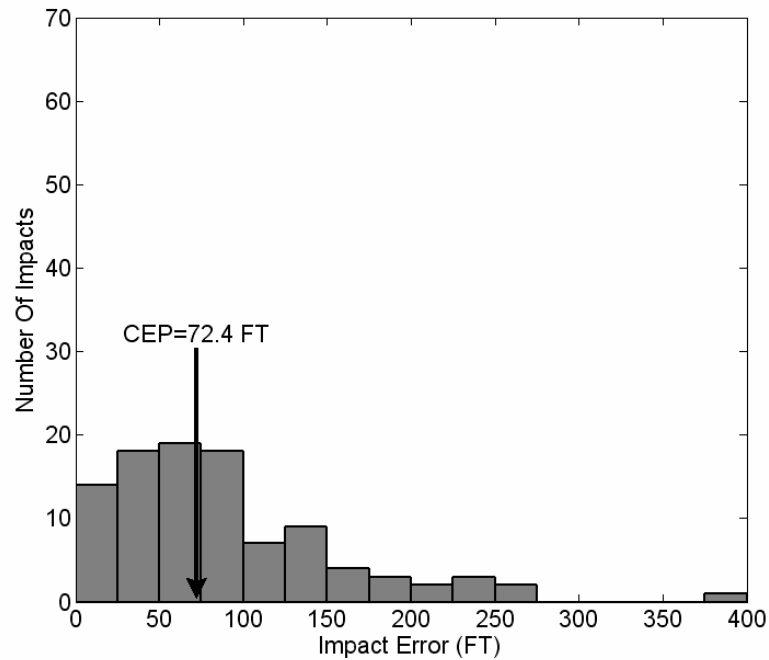
Fig. 28 Dispersion for All Sensor Errors and Varying Wind

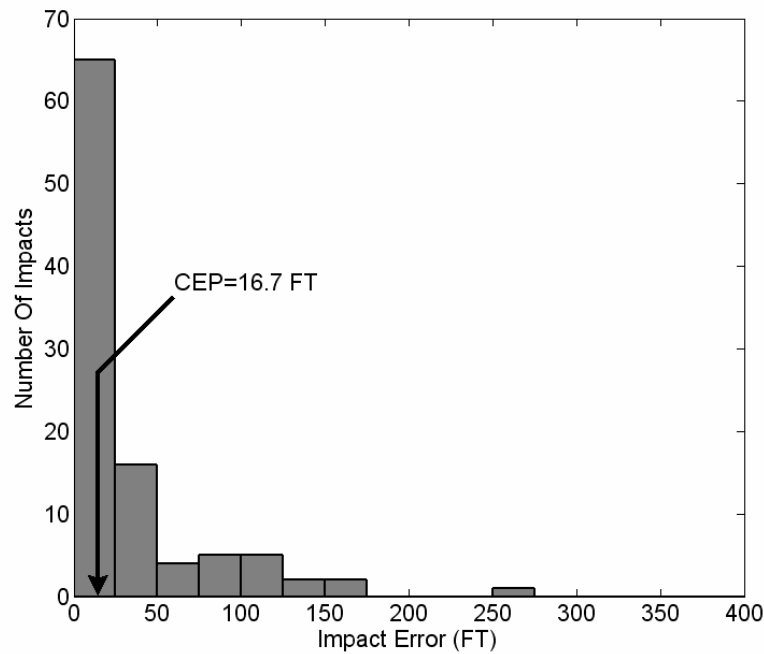Fig. 29   No GS Control Histogram for Sensor Errors and Varying Winds

American Institute of Aeronautics and Astronautics

Fig. 30   GS Control Histogram for Sensor Errors and Varying Winds

VI.   Conclusions

The ground station GUI developed under this project provides a flexible interface between a laptop ground station and a micro air vehicle autopilot. An example of the user friendly features of this interface is the manner in which a route is defined. The interface permits route waypoints to be defined manually or entered graphically through a map within FalconView. The route can be saved and uploaded to the autopilot. Through automation, the current position of the autopilot can be drawn on a map within FalconView so the user has an idea of the vehicles location with respect to the uploaded waypoints. In addition, the plotting feature allows the user to see the incoming sensor data versus time.   All these new features make programming and using the autopilot easier and more informative for the end user. Accomplishments include:

- Developed a program which allows the autopilot to be programmed through a user friendly interface.
- The GUI allows route waypoints to be defined in FalconView and then sent to the autopilot.
- The GUI allows the current position of the autopilot to be displayed on a FalconView map.
- The GUI allows sensor data to be displayed versus time as it is received from the autopilot.

An innovative new technique to achieve direct longitudinal control through dynamic incidence angle changes was created. Addition of this extra control channel requires simple rigging changes and an additional servo actuator. The ability of dynamic incidence angle to alter the glide slope of a parafoil and payload aircraft was demonstrated through a flight test program with a micro parafoil system. Results from the flight test program were synthesized and integrated into a 6 degree-of-freedom simulation. The simulation model is subsequently used to assess the utility of glide slope control to improve autonomous flight control system performance. Through Monte Carlo simulation, impact point statistics with and without glide slope control indicate that dramatic improvements in impact point statistics are possible using direct glide slope control. Accomplishments include:

- Created a new technique to directly control glide slope of an autonomous parafoil and payload aircraft called dynamic incidence angle.
- Demonstrated the ability of dynamic incidence angle control of a parafoil to provide reliable glide slope changes.

American Institute of Aeronautics and Astronautics

• Showed that incorporation of dynamic incidence angle control of a parafoil and payload aircraft can improve impact point accuracy by a factor of 3.

The GUI developed under this project has been delivered to the U.S. Army Research Laboratory for use in their micro air and ground vehicle research.

References

[1] Slegers, N., and Costello, M., "Aspects of Control for a Parafoil and Payload System," *Journal of Guidance, Control, and Dynamics*, Vol 26, No 6, pp 898-905, 2003.

[2] Ware, G., and Hassell, J., "Wind-Tunnel Investigation of Ram-Air_Inflated All-Flexible Wings of Aspect Ratios 1.0 to 3.0," NASA TM SX-1923, 1969.

[3] Brown, G., "Parafoil Steady Turn Response to Control Input," AIAA Paper 93-1241, May, 1993.

[4] M. Hailiang, and Q. Zizeng, "9-DOF Simulation of Controllable Parafoil System for Gliding and Stability," *Journal of National University of Defense Technology*, Vol. 16 No. 2, 1994, pp. 49-54.

[5] DeTurris, D,. Ervin, J., and Alptekin, S., "Development of an Autonomous Tactical Reconnaissance Platform," AIAA-2003-2117, May 2003.

[6] Altmann, H., and Windl, J., "ParaLander: A Medium-weight Demonstrator for Autonomous, Range-optimized Aerial Cargo Delivery," AIAA-2005-1627, May 2005.

[7] Jann, T., "Advanced Features for Autonomous Parafoil Guidance, Navigation and Control," AIAA-2005-1642, May, 2005.

[8] Bennett, T., and Fox, R., "Design, Development & Flight Testing of the NASA X-38 7500 ft2 Parafoil Recovery System," AIAA-2003-2107, May 2003.

[9] Madsen, C., Sostaric, R., and Cerimele, C., "Flight Performance, Aerodynamics, and Simulation Development for the X-38 Parafoil Test Program," AIAA-2003-2108, May 2003.

[10] George, S., Carter, D., Berland, J., Dunker, S., Tavan, S., and Barber, J., "The Dragonfly 4,500 kg Class Guided Airdrop System," AIAA-2005-7095, Sep. 2005.

[11] Zhu, Y., Moreau, M. Accorsi, M., Leonard, J. and Smith, J., "Computer Simulation of Parafoil Dynamics," AIAA 2001-2005, May 2001.

[12] Gupta, M., Xu, Z., Zhang, W., Accorsi, M., Leonard, J., Benney, R., and Stein. K., "Recent Advances in Structural Modeling of Parachute Dynamics," AIAA 2001-2030, May 2001.

[13] Iacomini, C., and Cerimele, C., "Lateral-Directional Aerodynamics from a Large Scale Parafoil Test Program," AIAA Paper 99-1731, Jun. 1999.

[14] Iacomini, C., and Cerimele, C., "Longitudinal Aerodynamics from a Large Scale Parafoil Test Program," AIAA Paper 99-1732, Jun. 1999.

[15] Lamb, H., Hydrodynamic*s*, Dover Publications, New York, 1945, pp 160-174.

[16] Lissaman, P., and Brown, G., "Apparent Mass Effects on Parafoil Dynamics," AIAA Paper 93-1236, May, 1993.

[17] Barrows, T., "Apparent Mass of Parafoils with Spanwise Camber," *Journal of Aircraft*, Vol 39, No 3, 2002, pp 445-451.

[18] Slegers, N., Costello, M., "Model Predictive Control of a Parafoil and Payload System," *Journal of Guidance, Control, and Dynamics*, Vol 28, No 4, 2005, pp 816-821.